Accepted Manuscript

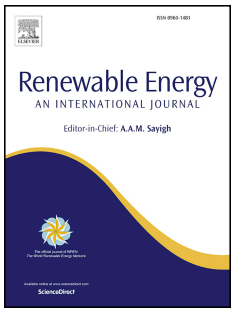

On the multi-scale interactions between an offshore-wind-turbine wake and the ocean-sediment dynamics in an idealized framework – A numerical investigation

T. Nagel, J. Chauchat, A. Wirth, C. Bonamy

PII: S0960-1481(17)30839-X

DOI: 10.1016/j.renene.2017.08.078

Reference: RENE 9176

To appear in: *Renewable Energy*

Received Date: 10 March 2017

Revised Date: 29 July 2017

Accepted Date: 26 August 2017

Please cite this article as: Nagel T, Chauchat J, Wirth A, Bonamy C, On the multi-scale interactions between an offshore-wind-turbine wake and the ocean-sediment dynamics in an idealized framework – A numerical investigation, *Renewable Energy* (2017), doi: 10.1016/j.renene.2017.08.078.

On the multi-scale interactions between an offshore-wind-turbine wake and the ocean-sediment dynamics in an idealized framework − a numerical investigation

T. Nagel[a,b], J. Chauchat[a,b], A. Wirth[a,b], C. Bonamy[a,b]

[a] *Univ. Grenoble Alpes, LEGI, F-38000 Grenoble, France*
[b] *CNRS, LEGI, F-38000 Grenoble, France*

Abstract

We investigate the turbulent dynamics of the coupled atmosphere-ocean-sediment system around a wind turbine. To this end, a coupled two-dimensional idealized numerical model of the ocean and sediment layers, forced by an idealized offshore wind turbine wake is used. The turbine wake impacts the ocean surface and for strong wind and water layer thickness higher than 20m, large scale eddies of the size comparable to the wake thickness are generated, leading to a turbulent dynamics in the ocean. The turbulence in the ocean is controlled by the shallow wake parameter S. The turbulent ocean dynamics is numerically integrated using time dependent simulations at fine horizontal resolution (1m). From these simulations, eddy coefficients parametrizating the turbulent fluxes are proposed to be used in larger-scale (RANS) models. The ocean dynamics and the parameter values depend mainly on S.
The ocean dynamics is laminar ($S>7.10^{-2}$), has a localized ($7.10^{-2} <S<7.10^{-2}$) or domain wide turbulent ($S<3.10^{-2}$) behavior. In the first two cases, changes in seabed elevation are around a few millimeters per month. For the third case, averaged over several days, changes decreases to a few tenths of millimeters per month. This is due to the alternating local velocity which transports sediments back and forth.

Keywords:
offshore-wind-turbine, wake, sea-sediment interactions, ocean dynamics, seabed dynamics

1. Introduction

Because of the rising need for sustainable energy and because wind energy is one of the few forms of renewable energy that can be harvested efficiently, many countries are planning and building offshore wind farms to increase the proportion of renewable energy in their energy mix. According to the European Wind Energy Association 2013 annual report [1], the installed European

*Corresponding author
Email address: tim.nagel@univ-grenoble-alpes.fr (T. Nagel)

capacity was of 5 GW at the end of 2012. By 2030, the European offshore wind capacity could totalize 150 GW, corresponding to 14% of the actual EU's total electricity consumption.

This offshore wind energy development growth is worldwide and faces several ecological, technical and scientific issues. First of all, wind energy installations are not free from environmental impacts, on coastal and marine ecosystems (a recent literature review on the subject is given by Dai [2]) but also on the seabed evolution. The latter is affected by a scour process due to the pile presence, a phenomenon similar to that occurring at bridge piers (e.g [3], [4], [5]). This scour phenomenon may be responsible for the turbid sediment wakes behind individual monopile recently observed ([6]). It has also been shown that local seabed elevation is affected by the piles presence in offshore wind farms [7]. On a larger scale, the impact of wind farms on the European regional climate [8] or on hurricanes [9] have been studied recently, showing that the wind farms environmental impacts are an important question nowadays. For economic reasons, trustworthy power predictions are needed before implementing a wind farm. According to Archer [10], research advancements in offshore observation, wind power forecasting, and turbulent wake loss would improve the models used and thus the power predictions for a given site.

To the best of our knowledges, the major part of atmospheric numerical models around wind turbines do not implement the ocean as a moving boundary but as an inert one with a constant roughness, the currents and the wave dynamics are thus neglected. Moreover, a recent numerical study from Moulin and Wirth [11] demonstrated that, at the sub-meso (O(10km)) scale, the oceanic currents are important in air-sea interactions and leave an imprint in the atmospheric dynamics.

Finally, if recent studies have shown the influence of large wind farms on the upper ocean circulation [12] or the influence of the turbine monopile on the local ocean and seabed dynamics ([13], [14]), no work has been done on the atmospheric wake's impact on the ocean-sediment dynamics and on a possible feedback on the atmosphere. The purpose of the present paper is to answer the following questions: (i) What is the wake's impact on the ocean-sediment dynamic? (ii) Is it possible to parametrize it for future upscalling developments? (iii) Have the ocean and sediment dynamics a feedback on the atmospheric energetic budget?

An idealized 2D numerical model has been built in order to answer these questions. In Section 2, the physical model and the basic equations that describe the mathematical model are detailed. The numerical model proposed and the different runs undertaken are described in Section 3. Section 4 is devoted to a presentation of the results, which are discussed in Section 5. The conclusions and perpectives are given in Section 6.

2. Physical and Mathematical Model

The physical model consists in two superposed layers (figure 1.a), a homogeneous shallow water ocean layer above a sediment bed layer, composed

of cohesion-less particles. The atmospheric layer is represented as an external forcing (F), which corresponds to the wake of wind turbines.

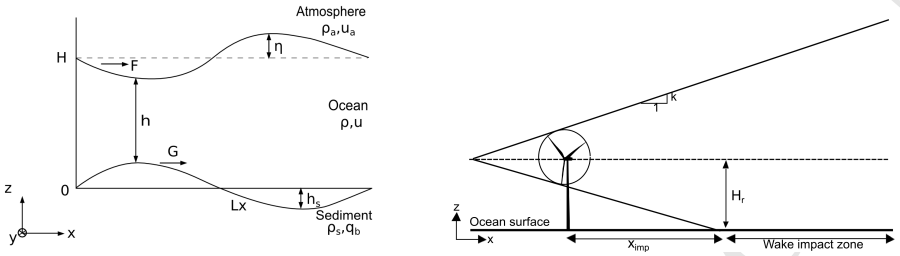

Figure 1: Sketch of the two layer physical model (a) and of the Jensen wake (b). All the variables are detailled in the text.

The domain length in the x-direction is denoted by L_x and by L_y in the y-direction. The average depth of the ocean layer is denoted as H and the bed load transport rate is denoted as q_b. The local thickness of the ocean layer and the seabed elevation, are denoted as $h(x, y, t)$ and $h_s(x, y, t)$, respectively. The free surface elevation is:

$$\eta(x, y, t) = h(x, y, t) - H + h_s(x, y, t). \tag{1}$$

The dimensional variables are consigned in the table 2. Densities are denoted as ρ, ρ_s and ρ_a for the ocean, the sediment and the atmosphere, respectively, d_s is the diameter of a sand grain. The ocean layer is forced by the local wind stress at its upper surface. The spatial variation of this wind stress incorporates the wake-profile of a wind turbine. The oceanic motion induces a shear stress τ_b on

Table 1: Domain parameters.

ρ (kg.m^{-3})	ρ_s (kg.m^{-3})	ρ_a (kg.m^{-3})	L_x (m)	L_y (m)	H (m)	d_s (μm)
1025	2650	1.2	10^3	10^3	10-50	200

the sediment bed layer. This stress and the seabed elevation are responsible for the coupling between the ocean and the sediment bed layers.

2.1. Hydrodynamic model

Mathematically, the ocean dynamics is given by the two dimensional Shallow Water (SW) equations [15, 16]. Most of the wind farms are localized in coastal areas, in 2012 for example, the average water depth of offshore wind farms was of 22m [1]. These equations are therefore considered to be adequate to describe the problem:

$$\partial_t \vec{u} + (\vec{u} \cdot \nabla)\vec{u} + g\nabla\eta \;=\; \nu\nabla^2\vec{u} + \vec{F} - \vec{G} \tag{2}$$

$$\partial_t h + \nabla(h\vec{u}) \;=\; 0, \tag{3}$$

where g is the gravitational acceleration, $\vec{u}\begin{pmatrix} u \\ v \end{pmatrix}$ is the velocity vector and ν is the kinematic viscosity. Finally, $\vec{F}$ and $\vec{G}$ correspond to the frictionnal accelerations applied on the ocean layer by the atmosphere (wind stress) and the sediment (bottom shear stress), respectively. They are characterized by a quadratic friction law [17]:

$$\vec{F} = \frac{1}{\rho h}\ \vec{f}, \tag{4}$$

where $\vec{f}$ is the shear stress applied to the ocean. It is calculated using the velocity difference between wind and ocean current as described by Moulin and Wirth [11]:

$$\vec{f} = C_{Da}\ \rho_a\ ||\ \vec{u}_{10} - \vec{u}\ ||\ (\vec{u}_{10} - \vec{u}), \tag{5}$$

where $||\ \vec{u}_{10} - \vec{u}\ ||$ is the magnitude of the velocity difference between the atmospheric velocity at 10m above the sea surface and the ocean current. In this work $u_{10} \in [10; 20]$ m/s and is directed in the positive x-direction. The drag coefficient C_{Da} follows Wu [18] and Smith [19]:

$$C_{Da} = (0.6 + 0.07u_{10})\ 10^{-3} \quad \text{for } \mathrm{u}_{10} \in [6; 26]\mathrm{m/s}. \tag{6}$$

The validity range of this friction law corresponds to the good working conditions of wind turbines, from 4 $\mathrm{m.s^{-1}}$ to 25 $\mathrm{m.s^{-1}}$. A similar quadratic friction law is used to model the friction between the ocean and the sediment layers:

$$\vec{G} = \frac{1}{h}\ \vec{\tau_b}, \tag{7}$$

$$\vec{\tau_b} = C_D\ \ ||\ \vec{u}\ ||\ \vec{u}, \tag{8}$$

with $||\ \vec{u}\ || = \sqrt{u^2 + v^2}$ and $C_D = 0.005$ the friction coefficient between the sediment bed and the ocean. This approach parametrizes the wave-current boundary layer and the effect of bedform roughness, but does not take into account the local roughness variations in space and time [20].

Under strong wind conditions, when the sea surface is rough, vertical turbulent density fluxes are high, especially near the surface. This reduces the vertical shear and the stratification in the surface-mixed-layer. It has a depth up to 50m in the ocean [21]. In the dynamics of eddies, the pressure exerted by the free-surface has a governing role. In an unstratified ocean, under the hydrostatic approximation,the vertical penetration of the pressure is comparable to the horizontal extension of the eddy [16]. In the cases considered here, eddies extend over the total depth.

2.2. Morphodynamic model

For an oceanic bed composed of cohesionless grains (sand), the sediment starts to move when the drag force exerted by the flow is higher than the friction force between the grains. The dimensionless Shields parameter [22], gives the ratio between the drag force and the apparent submerged grains weight:

$$\theta = \frac{\tau_b}{(\rho_s - \rho) g d_s}, \tag{9}$$

The sediment starts to move as soon as the Shields parameter exceeds a critical value ($\theta > \theta_c$), which depends on the density and the grain size.
Variability of the bed motion results from a local flux balance described by the Exner [23] equation:

$$\partial_t h_s(x, y, t) + \vec{\nabla} \cdot \vec{q}(x, y, t) = 0, \tag{10}$$

where h_s is the bed elevation and $\vec{q}$ is the total sediment flux.
Two modes of sediment transport exist, bedload transport and suspended load transport. In this work, only the bedload transport will be considered, this type of transport is generally dominating for rather low values of the bed shear stress, i.e when the Shields parameter of the flow is just above the critical value.
If only bedload transport is considered, the total sediment flux becomes:

$$\vec{q} = \frac{1}{1-p}\, \vec{q}_b, \tag{11}$$

where p=0.5 is the bed porosity and $\vec{q}_b$ is the bed load transport rate.
In the present model, the Meyer-Peter and Müller (MPM) [24] transport formula is used to describe the bed load transport rate q_b. It relates the latter to the excess Shields parameter:

$$\frac{q_b}{d_s \sqrt{(\rho_s/\rho) g d_s}} = \begin{cases} 8(\theta - \theta_c)^{3/2} & \text{if } \theta > \theta_c \\ 0 & \text{otherwise} \end{cases}. \tag{12}$$

2.3. Turbine wake model

The turbine wake affects the ocean by modifying the surface shear in the region where the wake intersects the ocean surface (see figure 1.b). This perturbation is maximal at the impact location, x_{imp} and then decreases downstream until vanishing. The wake model used in this work describes the velocity deficit induced by the rotor in the far wake region. The simplest model is given by Jensen [25], assuming a linearly expanding or cone wake with a velocity deficit that only depends on the distance from the rotor.

$$u_{10} = U_\infty \left[1 - \frac{1 - \sqrt{1 - C_w}}{(1 + 2kx/D)^2} \right], \tag{13}$$

where U_∞ is the wind velocity far from the turbine, C_w is the drag coefficient between the turbine and the air and k is the Wake Decay Constant. The standard Wake Decay Constant recommended in the WAsP help facility [1] is k=0.05 for offshore wind turbines. .

The wake impacts the ocean surface at a given distance downstream from the rotor position (figure 1.b). For the Jensen's model we have:

$$x_{\text{imp}} = \frac{H_r - D_r/2}{k} \tag{14}$$

This impact distance x_{imp} depends on the wind turbine height and on the rotor diameter and is increasing with the turbine size. For the turbines considered here ($H_r = 70$m and $D_r = 80$m, $k = 0.05$), the impact distance is 600 meters, several times the turbine height. Perturbations in the seabed induced by the turbine pile are localized in the pile vicinity. The pile diameter doesn't exceed 5 meters for the type of turbine considered. Furthermore, the perturbations due to the pile can extend up to 200m downstream in the oceanic layer [13], which is still significantly less than the wake impact distance. The seabed perturbations induced by the pile and the wake presence are thus uncorrelated provided that the spacing between two consecutive turbine is larger than the impact distance. Finally, the order of magnitude of the drag forces deficit induced by the wake (≈100kN) on the flow is at least one order of magnitude larger than the one induced by the pile (≈5kN). The effect of the pile is therefore not considered in the present work.

The Jensen wake model boundaries are extremely sharp, indeed, the velocity difference between inside and outside the wake corresponds to a step function. Such sharp boundaries are unrealistic and are prone to generating artificial instabilities. To be more realistic without changing the large scale characteristic of the wake model, we used a gaussian mollifier (also known as approximation to the identity) function with a characteristic mollify length L_m.

2.4. Non-dimensional equations

The SW equations (2) and (3) can be made dimensionless by the length scale D (the wake diameter at the impact location) for the horizontal direction, H (the average ocean layer thickness) for the vertical one, by U (the unperturbed flow velocity) for the velocity scale and by D/U for the timescale.
The SW equations can thus be rewritten as:

$$\begin{aligned} \partial_{t^*}\vec{u^*} + (\vec{u^*}\cdot\nabla^*)\vec{u^*} + \frac{H}{D}\frac{1}{{F_r}^2} g^*\nabla^*\eta^* \;=\; \\ \frac{1}{R_e}\nabla^{*2}\vec{u^*} + \underbrace{\frac{S_a}{\rho\, h^*}\,\rho_a \,||\, \vec{u}^*_{10} - \vec{u^*} \,||\, (\vec{u}^*_{10} - \vec{u^*})}_{\overline{F^*}} - \underbrace{\frac{S}{h^*}\;||\,\vec{u^*}\,||\,\vec{u^*}}_{\overline{G^*}} \end{aligned} \tag{15}$$

[1] *www.wasp.dk*

$$\partial_{t^*} h^* + \nabla^*(h^* \vec{u^*}) \; = \; 0, \tag{16}$$

where $F_r = \dfrac{U}{\sqrt{gD}}$ and $R_e = \dfrac{UD}{\nu}$ are the Froude and the Reynolds numbers, respectively. Furthermore, in the non-dimensionnal bottom friction acceleration $\overline{G^*}$ an other dimensionless number appears, denoted as S. It is the so-called "wake stability parameter" introduced by Ingram and Chu [26], or Chen and Jirka [27, 28]:

$$S = \frac{C_D D}{H} \tag{17}$$

The S parameter compares the bottom friction to the advection terms. S is a control parameter of the wake instabilities in shallow water flows, it has been used in the case of an island in a bay [26] or in laboratory experiments [27].
A similar parameter (S_a) appears in the non-dimensionnal atmospheric forcing but its effect on the eddy dynamic is small. Indeed, the wind shear mainly depends on the (imposed) wind velocity and only weakly on the ocean velocity. It will therefore not be discussed in the present paper.

3. Numerical model

3.1. Structure of the numerical model

Written in Fortran 90, the overall model can be divided in two coupled modules, the hydrodynamic and the morphodynamic modules. They are subject to input data, such as atmospheric forcing and bedform elevation. The hydrodynamic module solves the SW equations and is spatially discretized using the centered finite difference method and temporally discretized using a second order Runge-Kutta scheme (see [29], chapter 4). Output from this module are the velocity fields u and v along with the free surface elevation η. These velocity fields are necessary to compute the Shields number. The morphodynamic module is only called if the Shields number exceeds the critical value in one or more of the grid points. The morphodynamic module solves the Exner equation using a NOCS (Non-Oscillatory Central Scheme) scheme as described by Jiang et al. ([30], [31]) (see Appendix).
As the morphological timescale is large compared to the to hydrodynamic one, two time-steps are used, one for the hydrodynamic module (Δt) and the other for the morphodynamic module with $\Delta t_{morpho} = 1000 \times \Delta t$. The value of n_{morpho}=1000 has been determined based on a 1D benchmark consisting of the advection-diffusion calculation of a sand dune by a current. This test case has been inspired from Marieu[32]. Furthermore, having a large morphodynamics time-step allows to reduce the diffusion of the NOCS scheme and save computational time.
The organization chart of the code can be found in figure 2 and all the input parameters are given in table 2.

3.2. Numerical Grid, Boundary Conditions and Stability Criterion

The ocean and the sediment are considered in a rectangle of size $L_x \times L_y$. For eddy resolving simulations (consigned in table 3) the numerical grid is regular and contains $n_x \times n_y$ points, with $n_x = 1997$ when $L_x = 2000$m and $n_y = 597$ or 997 when $L_y = 600$m or 1000m, respectively. For these configurations, the spatial resolution is around 1m in both horizontal directions.

For the shallow water and the morphological modules, the variables value calculated at grid point i involves values at points $i-1$ and $i+1$, if we consider one direction only. Thus, at the boundaries, values of each variable have to be given. Here, periodic boundary conditions are used. Every point which is coming out of the domain at a boundary reappears at its opposite side. The same process is applied in the second horizontal direction.

Concerning the stability of the numerical scheme, the Courant-Friedrichs-Lewy criterion (CFL) has to be satisfied for the ocean and sediment layers. While ocean waves propagation celerity is classically defined as $c_{ocean} = \sqrt{gh}$ (with h being the ocean layer thickness), sand waves propagation celerity (c_{sand}) corresponds to the dunes migration speed. As in the model $h \in [15; 60]$ m, $c_{ocean} \in [12; 24]$ m.s^{-1} and $c_{sand} \approx 10^{-4}$ m.s^{-1}, if the CFL conditions for the ocean is satisfied, it is also the case for the morphodynamic CFL. The ocean thus set the maximum time step at $\Delta t = 0.02$s.

A global overview of the numerical experiments performed is given in table 3. In the reference case (H15) the water depth is 15m and the domain width is 600m. The rotor diameter and height, $D = 80$m, $H_r = 70$m, correspond to a Vestas V80−2.0 MW turbine, one of the most widespread offshore wind turbine. The wind speed 10 meters above the sea level (u_{10}) is equal to 20m.s^{-1}, corresponding to the high range of these turbines good working conditions [2]. Simulations have been undertaken for six different water layer thicknesses, 15, 20, 30, 40, 50 and 60m, and three different wind velocities (u_{10} =10, 15 and 20 m.s^{-1}). Run H20CD2P3 has a bottom friction coefficient $C'_D = (2/3)C_D$. Runs H20w, H30w, H40w, H50w and H60w have a domain width of 1000m in order to limit the lateral confinement. Finally, runs H60CD3P4 and H60wCD3P4 have a bottom friction coefficient $C'_D = (3/4)C_D$. For each case, the initial free surface and seabed elevation fields are set to zero.

Most of the results presented in the following section are obtained after 14 days of dynamic, when a statistically steady state has been obtained. As the code is parallelized using MPI it represents, for a 1000m domain width run, around 85 hours of computations on 128 Intel E5-2670 processors (approximatively 11k core hours).

[2] Vestas V80-2.0 MW product brochure: *http://www.vestas.com*

Table 2: Model input parameters.

Parameter	**Value (unit)**
temporal parameters	
Δt: time scale for ocean dynamics	0.02 (s)
n_{morpho}: time scale for morphodynamics ($\Delta t_{\text{morpho}} = n_{\text{morpho}} \times \Delta t$)	1000 (-)
n_{iter}: iteration number for one run	60 000 000 (-)
domain parameters	
L_x : Domain length in the x-direction	2000 (m)
L_y : Domain length in the y-direction	600 or 1000 (m)
H : Initial water depth	from 15 to 60 (m)
ocean parameters	
ρ : sea water density	1025 (kg.m^{-3})
C_{Da} : atmosphere/ocean friction coefficient	2.0×10^{-3} (-)
sediment parameters	
ρ_s : sediment density	2650 (kg.m^{-3})
d_s : sediment grain diameter	200 (μm)
C_D : ocean/sediment friction coefficient	from 3.3×10^{-3} to 5.0×10^{-3} (-)
atmosphere parameters	
ρ_a : atmosphere density	1.2 (kg.m^{-3})
u_{10} : input wind velocity	10, 15 or 20 (m.s^{-1})
wake and turbine parameters	
H_r : wind turbine hub height	70 (m)
D_r : wind turbine rotor diameter	80 (m)
k : slope of the linear Jensen wake model	0.05 (-)
C_w : wind turbine drag coefficient	0.87 (-)

4. Results

The first part of this section focuses on the wake impact upon the ocean dynamics, particularly with the generation of instabilities, while the second part is dedicated to the morphodynamics impact. Results of the numerical experiments are consigned in table 3.

4.1. Ocean dynamics

Figure 3 shows the vorticity fields ($\zeta = \partial_x v - \partial_y u$) in the oceanic layer after 14 days of dynamics for 15, 20, 30 and 50m of water layer thickness. The 15m water layer thickness case (H15, figure 3.a) has a laminar dynamics and the vorticity is higher (or lower) at the wake boundaries showing that they are high shear-stress zones. Figure 3 also shows that increasing the water layer thickness leads to a generation of oceanic instabilities. Indeed, for the 20 and 30m water layer cases (H20 and H30, figure 3.b and 3.c, respectively), vortices formed at the wake impact location continue to develop along the wake boundaries and form two distinct vortex streets. The eddies diameter (D_e) and spacing (L_e)

depend on the water layer thickness too (see table 3 or figure 4, representing the variations of the eddies diameter for the different numerical simulations undertaken), both increasing with an increasing water layer thickness. When the latter exceeds 40m, the vortex streets interact one with the other leading to a domain-wide turbulence.

For the 50m case (H50, figure 3.d) parts of the vortices are leaving the computational domain at one side and reenter at the opposite side due to the periodic boundary conditions. In order to ged rid of this confinement phenomenon, additional runs have been carried out with a wider domain of 1000m [H20w, H30w, H40w, H50w, H60w and H60wCD3P4]. From a physical point of view, the 1000m width cases can be seen as a lesser densely packed wind farm. For the H50w case (figure 3.e), because the confinement phenomenon is not occurring, the vortices shape is closer to the one observed for H30 than for H50. Finally, for all the water layer thicknesses where vortices are well formed (*i.e* from 30 to 60m), the presence of filaments inside the vortices is noteworthy. These filaments correspond to high shear-stress zones and appear initially at the wake boundaries. They are then advected in the x-direction and rotated around the vortices center. As these filaments intensity decreases with their advection and rotation they are slowly reduced by viscosity.

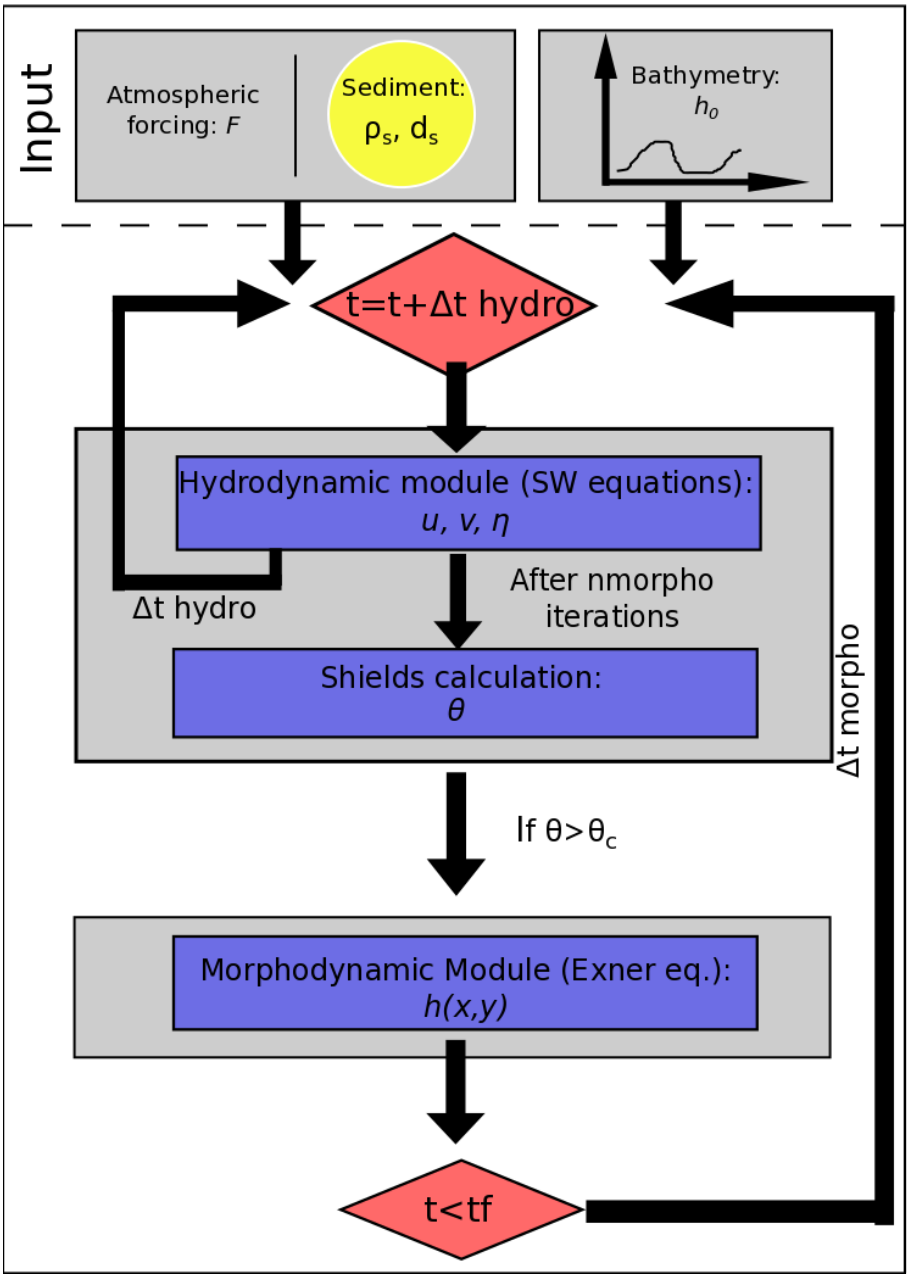

Figure 2: Flowchart of the solving procedure, $nmorpho = \Delta t_{morpho}/\Delta t$.

Table 3: Numerical experiments and results main parameters, S is the stability wake parameter, ΔU is the velocity difference between outside and inside the wake at the impact location, D_e is the eddies diameter, L_e is the eddies spacing, the maximum deposition and erosion values correspond to maximum seabed elevation (positive or negative, respectively) noticed at the end of each run (14 days).

Run name	**H**	$\mathbf{L_y}$	$\mathbf{u_{10}}$	$\mathbf{C_D}$	$\mathbf{D_r}$	**S**	ΔU	$\mathbf{D_e}$	$\mathbf{L_e}$	**Max deposition**	**Max erosion**
Unit	**m**	**m**	$\mathbf{m.s^{-1}}$	$\mathbf{(10^{-3})}$	**m**	$\mathbf{(10^{-2})}$	$\mathbf{m.s^{-1}}$	**m**	**m**	**mm**	**mm**
H15	15	600	20	5	80	7.33	8.19	-	-	1.75	-2.12
H20	20	600	20	5	80	5.50	8.19	120	500	1.28	-1.61
H30	30	600	20	5	80	3.67	8.19	250	650	0.89	-1.10
H40	40	600	20	5	80	2.75	8.19	550	1000	0.74	-0.83
H50	50	600	20	5	80	2.20	8.19	550	1000	0.64	-0.66
H60	60	600	20	5	80	1.83	8.19	550	1000	0.56	-0.53
H60CD3P4	60	600	20	3.75	80	1.375	8.19	550	1000	0.54	-0.49
H20CD2P3	20	600	20	3.3	80	3.63	8.19	250	650	0.88	-1.07
H30Dr	30	600	20	5.	40	4.68	8.19	130	500	1.41	-1.52
H20w	20	1000	20	5	80	5.50	8.19	120	500	1.39	-1.50
H30w	30	1000	20	5	80	3.67	8.19	200	650	0.92	-1.02
H40w	40	1000	20	5	80	2.75	8.19	250	650	0.71	-0.77
H50w	50	1000	20	5	80	2.20	8.19	450	1000	0.62	-0.63
H60w	60	1000	20	5	80	1.83	8.19	580	1000	0.52	-0.52
H60wCD3P4	60	1000	20	3.75	80	1.375	8.19	600	1000	0.56	-0.47
H50U15	50	600	15	5	80	2.20	6.14	550	1000	0.17	-0.21
H50U10	50	600	20	5	80	2.20	4.10	550	1000	-	-

The confinement phenomenon can be highlighted thanks to the eddies diameter. Indeed, figure 4 shows that for larger domain width, the vortex size is slightly smaller for all the layer thicknesses from 30 to 50m. The largest difference between the confined and the unconfined situations is found between runs H40 and H40w: if run H40 is similar to run H50 in terms of vortex size, spacing and vorticity intensity, run H40w is closer to runs H30 and H30w. Qualitatively, two distinct vortex streets are formed in the domain for H40w rather than two interacting ones as for run H40. The explanation comes from a combination of confinement and periodic boundary conditions: the confinement leads to a slight increase of the Reynolds shear stress, thus of the turbulence intensity and of the eddies size. For the confined domain, at H=40m, the eddies diameter becomes more important than the half domain width and the periodic boundary conditions allow part of the vortices to leave the domain and reenter on the opposite side. The vortex streets are thus perturbed, deviated by the reentering vortices and both vortex streets start to interact one with the other leading to a domain-wide turbulence.
Figure 4 also shows that once the domain-wide turbulent state is reached, the eddies size remains constant when increasing the water layer thickness. Thus, for 60m water layer thickness the unconfined eddies become larger than the confined ones.

The computational variable allowing a quantitative characterization of the domain's turbulence for a given run is the Turbulent Kinetic Energy integral over the domain:

$$\langle TKE \rangle = \frac{1}{2} H \iint_A (u'^2 + v'^2)\, dA \ , \tag{18}$$

where A is the domain surface, and u' and v' are the velocity fluctuations, defined according to the Reynolds decomposition.
Figure 5 presents the normalized turbulent kinetic energy ($\langle \text{TKE} \rangle^* = \langle \text{TKE} \rangle / {u_{10}}^2$) versus the S parameter (see section 2.4) for the runs described in the table 3. It clearly appears that, for a given domain witdh, the $\langle \text{TKE} \rangle^*$ collapses as a function of the S parameter. The S dependency of the normalized TKE is shown by runs H20CD2P3 and H30Dr. Indeed, decreasing the bottom friction coefficient by a factor 2/3 in order to conserve S for the two cases with different water depth (H20CD2P3 and H30) gives very similar results on the normalized TKE but also on the oceanic vorticity field (not shown here). Furthermore, changing the S parameter by changing the wake diameter at the impact location (D), which is done in run H30Dr, also keeps the normalized TKE value on the same curve. This shows that the S parameter is a control parameter of the oceanic turbulent dynamics, even if a dependency on the wind turbine spacing remains. Furthermore, as the S parameter appears in the bottom-friction term in the SW equation (see eq. 19), when increasing the water layer thickness S is decreasing and the importance of bottom friction decreases, allowing for stronger instabilities to develop. This explains the phenomenon observed in

figure 3.

$$\vec{G} = \frac{1}{h}\,\vec{\tau_b} = \frac{S}{D}\;\;||\,\vec{u}\,||\,\vec{u}. \tag{19}$$

Concerning the dependency on the domain width, it can be seen that for a S parameter corresponding to 30m water layer thickness (S_{H30}) or less, the normalized TKE has the same values for both domain width. For S higher than S_{H30}, the normalized TKE is affected by the lateral confinement. At 40m water layer thickness (S_{H40}), because of the vortex streets destabilization, turbulence becomes domain-wide) and the normalized TKE is higher for the confined case. At H=50m, the turbulence becomes also domain-wide for the less confined situation, so the normalized TKE becomes higher than for the confined case. Finally, for increasing water depth, the less-confined situation values of the normalized TKE will remain higher and the difference with the more confined case will continue to grow. This result can be correlated with the eddies size variation presented in figure 4.

The topology of the oceanic flow is particular due to the forcing by the wind turbine wake. Indeed, vorticity is not created at a fixed point, through the contact with an object and the corresponding formation of a boundary layer, but it is instead continuously injected at the boundary of the atmospheric turbine-wake and advected downstream by the oceanic flow. This is clearly seen when inspecting movies (provided as additional online material) of the vorticity in the ocean, where a continuous formation of a vortex filament and its advection superpose.

For large values of the wake stability parameter (H $\leq$ 15m), two elongated vortex-filaments of opposite vorticity appear and the flow reflects the symmetry of the forcing with respect to the center-line (y=300m). For smaller values of the wake stability parameter (S $< 5.50\ 10^{-2}$) the vortex filaments role up through a Kelvin-Helmholtz instability and eddies appear. Initially the symmetry is conserved but after some time the two vortex streets interact leading to the classical alternating von Karmann vortex street, in which the symmetry of the forcing is recovered in the time averaged variables. Further downstream the vortex filaments have a spiral structure.

When the vortex filament reenters the domain, due to periodic boundary conditions, another filament is imprinted on top of the existing one. This mechanism leads to the particular spaghetti-type structure of the vorticity field (figure 3). The signature of the vortex filaments are also clearly seen in a cut through the vorticity field of figure 3 at x=1340 m shown in figure 6. The result is a particular type of turbulence, composed of generated and decaying vortex filaments, where both processes are co-located in space and continuous in time.

4.2. Sediment dynamics

Figure 7 shows the seabed elevation after 14 days of dynamics. For a given wind velocity (here u_{10}=20 m.s^{-1}), the qualitative spatial impact of the wake upon the seabed is similar for all the water layer thicknesses considered. The

impact can be described as follows: first, the oceanic velocity deficit induced by the wake leads to a sediment accumulation, *i.e* a dune (corresponding to the local wake width) is formed close to the impact location, between $x = 300$m and $x = 500$m. The same phenomenon occurs at the wake boundaries. Such formations are due to the non uniformity of the oceanic velocity field and thus of the local bottom shear stress. Downstream in the wake, the velocity deficit becomes less important, corresponding to a bottom shear stress that induces bed erosion. Outside the wake, the flow velocity is higher, increasing the bottom shear stress and the sediment transport, leading to the formation of a hole on each side of the dune. Further downstream, at $x = 1000$m, the velocity and the bottom shear stress decrease, the erosion stops and aggradation occurs.

However, from a quantitative point of view, the local seabed elevation at a given time and for a given wind forcing depends on the water layer thickness. Indeed, in figure 7 and in table 3 it is shown that the maximum values of seabed erosion and deposition are decreasing when increasing the water layer thickness. The explanation can be found by looking at the bathymetry variation in a short time interval ($\Delta t \approx 1$ h) as shown in figure 8. The spatial patterns of the morphodynamical evolution between the turbulent and the laminar cases are completely different. The oceanic vortices strongly affect the seabed morphodynamics. For 20 m water layer thickness with a laminar dynamics (figure 8.a), the bathymetry variations are similar to the seabed elevation variation after 14 days of dynamics and thus linear in time. This is not the case for water layer thickness from 30 m to 50 m (figure 8.b, and 8.c, respectively), the wakes imprint on the seabed is totally annihilated by the signature of the large scale vortices. The differences in vortex scale observed in the ocean is recovered in the seabed, showing that vortex formation in the ocean can have a significant impact on the seabed morphodynamics.

Considering the morphodynamical evolution, three cases are observed, depending on whether the ocean dynamics is laminar, has a localized (H20, H30) or a domain wide (H40, H50) turbulent behavior. In the first case, changes in seabed elevation are around a few millimeters per month. Results are similar for the localized turbulence case. For the domain wide turbulence case, instantaneous seabed changes are of the order of a few millimeters per month, whereas the transport averaged over several days decreases to a few tenths of millimeter per month. This behavior is easily explained by the oscillating local velocity which transports sediments back and forth leading to strong transport when averaged over short-time intervals but small transport when average over long-time intervals. It is important to notice that in this study only bedload is considered, the suspended load is neglected and may lead to underestimation of sediment transport. An increase of sediment transport, especially by suspension is not free of environmental issues as it increases the local turbidity and may reduce the light in the water column, affecting marine life ([33]).

The above observations also apply to the less confined simulations, in which, for each case maximum of deposition and erosion values are close to the corresponding confined case.

In the present model, the oceanic velocity depends on the wind velocity at 10 meters above the surface. The bottom shear stress depends on the oceanic velocity via the MPM threshold transport formula (eq. (12)), when the bottom shear stress is under the critical value, no bedload transport occurs. In the present configuration, such phenomenon appears for u_{10}=10 m.s^{-1}, meaning that in the idealized model presented here, under a given wind velocity, the wake presence has no impact on the seabed. These results are based on the assumption that the seabed is composed of sand, if mud is considered, then the suspended sediment transport would be way more important.

5. Discussion

5.1. Parametrization

The turbulent ocean dynamics presented in the previous section is obtained thanks to eddy-resolving time dependent simulations. These simulations are performed at fine horizontal resolution (1m). Such fine resolution simulations can not be performed at a larger-scale (regional-scale) where it has been shown that offshore wind farms presence influence the ocean dynamics ([12],[14]). The aim of this section is to propose an eddy viscosity model to be used in larger-scale RANS models. To this end we propose different parametrizations on a coarser grid where $dx = 26$m and $dy = 16$m.

The simplest parametrization proposed is a local model, in which advection and horizontal friction are neglected and the velocity field is calculated as a local equilibrium between the atmospheric forcing and the bottom friction:

$$u = \sqrt{\frac{C_{Da}\ \rho_a}{C_D\ \rho}}\ u_{10}\ . \tag{20}$$

The parametrization of the turbulent ocean dynamic can also be undertaken using the Reynolds-averaged Navier-Stokes equations, denoted as RANS equations. The RANS simulations solve the time-filtered SW equations. Thanks to Reynolds decomposition, an instantaneous quantity (such as u) is decomposed into its time-averaged ($\overline{u}$) and fluctuating (u') part:

$$u = \overline{u} + u' \tag{21}$$

The two types of RANS parametrizations undertaken in the present work are the simplest possible, involving a constant eddy viscosity and a mixing length approach. This is consistant with state of the art coastal morphodynamics models.

From eddy resolving simulations, the eddy viscosity ν_{eddy} can be obtained a posteriori using:

$$\nu_{\text{eddy}} = -\frac{\overline{u'v'}}{\partial_y \overline{u}}\ , \tag{22}$$

where $\overline{u'v'}$ is a component of the Reynolds stress tensor and $\partial_y \overline{u}$ is the horizontal transverse gradient of the mean flow velocity (see figure 9). Once determined

from a fine resolution eddy resolving numerical simulation, the ν_{eddy} constant is simply added in the viscosity term in the equations of a coarse resolution simulation, which then rapidly converges to a stationary state.
For the Mixing Length L_m approach, the eddy viscosity can be written as:

$$L_m = \frac{\sqrt{|\ \overline{u'v'}\ |}}{|\ \partial_y \overline{u}\ |} \text{ and } \nu_{\text{eddy}} = |\ \partial_y \overline{u}\ |\ \ {L_m}^2. \tag{23}$$

The mixing length approach is more refined compared with a constant eddy viscosity. In this model, the eddy viscosity is space dependent and applied only where $\partial_y \overline{u}$ is important, *i.e* in the high shear stress zones, where the eddies are located.
All the three models presented above are compared with the eddy resolving results in order to determine their accuracy and efficiency. A y−direction transect of the mean velocity field is shown in figure 9. It clearly appears that for all the water layer thicknesses considered, the local model is far from the eddy resolving simulations, whereas both RANS models are very close to it, especially for larger water layer thicknesses (i.e for stronger turbulence states). These results may easily be explain by the hypothesis underlying each parametrization: the local model doesn't take into account the momentum transport, which is present in both RANS simulation and appears to be important in the dynamics. Furthermore, by looking at both, the 20m and the 50m water layer thickness cases, it appears that for $\overline{u}$, both RANS approaches give similar results. This is not the case when the shear is considered (left panel on figure 9), where the use of a mixing length gives better results than a constant eddy viscosity model, at least for the lowest water layer thickness. For the 20m water layer thickness the eddies are localized whereas they are domain wide in the 50m case, an eddy viscosity resulting from a local varying mixing length approach is thus not surprisingly better for the shallow cases than using a constant eddy viscosity.

Nevertheless, if a RANS parametrization seems to give satisfactory results this is only an a-posteriori parametrization, meaning that for each set of parameters an eddy resolving simulation is required to obtain the corresponding eddy viscosity or mixing length. In figure 10, the dimensionless eddy viscosity $\nu^*_{\text{eddy}} = \nu_{\text{eddy}}/D\ u_{10}$ is plotted versus the S parameter. For a given domain width, ν^*_{eddy} collapses on a master curve as a function of the S parameter. As the shear stress is higher in the confined situation it leads to higher values of ν^*_{eddy}. Consistently with the observation made in section 4.1, there is no confinement for H=20m. The dimensionless eddy viscosity is the same for both, the wide and the narrow domain.
For each domain width, a phenomenological law can be fitted to the data points. We propose a hyperbolic tangent function for $\nu^*_{\text{eddy}}(S)$:

$$\nu^*_{\text{eddy}}(S) = A\frac{1}{2}\left[1 + tanh\left(\frac{B-S}{C}\right)\right] \tag{24}$$

For the two situations considered here, the values of coefficients A, B and C are consigned in table 4.

Table 4: Numerical values of parameters A,B and C involved in eq. (24).

Situation	A	B	C
Confined	$1.173\ 10^{-4}$	$3.119\ 10^{-2}$	$7.420\ 10^{-3}$
Less confined	$1.200\ 10^{-4}$	$2.0\ 10^{-2}$	$1.0\ 10^{-2}$

The numerical values of the parameters A, B and C are different for each domain width. In this way, the correspondant eddy-viscosity function of S can only be applicable for a given domain width. Indeed, as show on figure 9, running a confined case RANS simulation with parameter value obtained from the less confined case gives satisfactory results on the mean velocity field $\overline{u}$, but not for the shear stress. The latter highligths the predominance of advection terms in the problem.

5.2. Atmospheric energy budget

The source of the oceanic mechanical energy is the shear between the atmosphere and the ocean. The atmosphere looses energy due to the friction with the ocean surface. The power lost by the atmosphere (P_{tot}) is the integral over the domain of the product between the wind stress and the wind velocity.

$$P_{\text{tot}} = C_{Da}\rho_a \iint_A || \vec{u_{10}} \tag{25}$$

Several hypothesis lead to a simplification of the energy budget computation and are presented hereafter: first of all, the y components of the velocity vectors can be neglected. Indeed, they are vanishing for the atmosphere and subdominant in the ocean ($v \ll u, u_{10}$), eq. (25) can be approximated by:

$$P_{\text{tot}} \approx C_{Da}\rho_a \iint_A \mid u_{10} - u \mid (u_{10} - u)u_{10}\ dA. \tag{26}$$

Furthermore, as the velocity in the atmosphere is always larger than in the ocean ($u_{10} > u,\ \forall x,\ \forall y,\ \forall t$) we have:

$$P_{\text{tot}} \approx C_{Da}\rho_a \iint_A (u_{10} - u)^2 u_{10}\ dA. \tag{27}$$

The power taken up by the ocean (P_{o}) is the integral over the domain of the product between the wind stress and the ocean velocity. Using the above simplifications, it can be written as:

$$P_{\text{o}} \approx C_{Da}\rho_a \iint_A (u_{10} - u)^2 u\ dA. \tag{28}$$

Furthermore, the total power taken out of the atmosphere can be seen as the sum of the one lost into friction and the one taken up by the ocean itself. The latter is also composed of two terms, the power taken by the mean flow (P_{mean}) and the one taken by the turbulent fluctuations (P_{turb}):

$$P_{\text{tot}} = P_{\text{fric}} + \underbrace{P_{\text{mean}} + P_{\text{turb}}}_{P_{\text{o}}} \tag{29}$$

Computations have been undertaken using the different eddy resolving and RANS models described in the previous section to quantify the energy transfer, the results are presented in figure 11. First of all, the results show that for all the cases investigated, the power taken by the ocean from the atmosphere is several orders of magnitude lower than the one lost by the atmosphere. The major part of the power lost by the atmosphere is thus dissipated through friction between the atmosphere and the ocean. Furthermore, taking into account the ocean velocity in the wind forcing leads to a decrease by 4% of the power lost by the atmosphere (comparison between cases with u=0 and the other ones in figure 11.a). It must be kept in mind that the influence of the ocean dynamics on the energetic budget may be different with an oceanic current that is not only forced by a local wind but due to a large scale or a tidal current.
Figure 11 shows that for the power taken out from the atmosphere and the power taken up by the ocean, the values estimated with the local model are close to the ones given by the eddy resolving model. The differences between the two models are of the order of 0.001% for the power lost by the atmosphere and of the order of 0.03% for the power received by the ocean, showing that the oceanic turbulence, which is not present in the local model, has a subdominant role in the air-sea energetic budget balance.

An analytical development can confirm and explain the above observations. The time average equation (27) can be written for laminar and turbulent oceanic flows:

$$\overline{P_{\text{tot}}} = C_{Da}\rho_a \iint_A \underbrace{{u_{10}}^3}_{a_1} \underbrace{-2{u_{10}}^2\overline{u} + u_{10}\overline{u^2}}_{a_2} + \underbrace{u_{10}\overline{u'^2}}_{a_3}\, dA, \tag{30}$$

where $\overline{u}$ is the mean flow velocity and $\overline{u'^2}$ is the square of the velocity fluctuations, or the streamwise component of the Reynolds stress tensor. If the flow is laminar, $\overline{u'^2} = 0$ and thus $a_3 = 0$.
The same procedure can be applied to the energy taken up by the ocean eq. (28) and gives for laminar and turbulent oceanic flows:

$$\overline{{P_{\text{o}}}^t} = C_D\rho_a \iint_A \underbrace{{u_{10}}^2\overline{u}}_{o_1} \underbrace{-2u_{10}\overline{u^2} + \overline{u^3}}_{o_2} + \underbrace{\overline{u'^2}(3\overline{u} - 2u_a)}_{o_3}\, dA\ . \tag{31}$$

Equations (30) and (31) highlight the importance of the different terms in the air-sea energetic balance. The term $o_1 = {u_{10}}^2\overline{u}$ is linked to the power taken by

the ocean without taking into account the oceanic velocity in the atmospheric forcing. This term is predominant in laminar and turbulent equations. The terms $a_2 = -2{u_a}^2\overline{u^2} + u_a\overline{u^2}$ and $o_2 = -2u_{10}\overline{u^2} + \overline{u^3}$ correspond to mean flow correction occurring when the oceanic velocity is taking into account in the atmospheric forcing. As the velocity in the atmosphere is always much larger and in the same direction than in the ocean, these correction terms are negative here. Taking into account the oceanic velocity in the atmospheric forcing reduces the shear and thus leads to a reduction of both P_{tot} and P_{o}. The terms $a_3 = u_{10}\overline{u'^2}$ and $o_3 = \overline{u'^2}(3\overline{u} - 2u_{10})$ correspond to the contributions of the turbulent fluctuations in the energetic balance. We have $a_3 > 0$ and $o_3 < 0$, for the idealized situation considered here. When turbulence occurs, it increases the power lost by the atmosphere but decreases the one received by the ocean. This can be explained by the fact that a part of the turbulent fluctuations is not in the same direction as the oceanic motion and the atmospheric forcing and increases the friction between the two layers. Furthermore, these fluctuations certainly reduce the energy transfer efficiency to the mean flow which may explain that they decrease the power received by the ocean.

6. Conclusion & Perspectives

An idealized 2D numerical model has been proposed to study the impact of an offshore wind turbine wake on the ocean and sediment dynamics. To the best of our knowledge, no study has ever been done on this subject so far. A simplified physical model has been proposed and a mathematical model has been built and solved numerically.

The results show that the turbine wake has an impact on both the ocean and the sediment bed layers. Turbine wake impact on the ocean surface can generate instabilities and vortex streets. Size and spacing between these vortices are controlled by the wake stability parameter $S = C_D D/H$. When S is decreased, large scale instabilities are more easily generated, leading to a domain wide turbulence state in the ocean. Furthermore, the results have also highlighted the important role of the confinement (the spacing of wind turbines in a farm) in the generation of instabilities.

The oceanic turbulence observed with eddy-resolving time dependent simulations can be parametrized using a simple zero equation RANS model: using a constant Boussinesq eddy viscosity in the shallow water equations, or using a mixing length approach. A phenomenological law for the non−dimensional eddy viscosity as a function of the S parameter has been proposed. This RANS parametrization of the turbulent oceanic dynamics allows for upscaling simulations (in a regional model, for example).

Concerning the seabed, it has been shown that the non-uniformity of the oceanic velocity field induced by the wake presence is observed in the local bottom shear stress responsible for sand erosion and deposition. As the vortices strongly affect the seabed morphodynamics, for localized and domain wide turbulence, the

wake imprint on the seabed tends to be reduced by large scale vortices and oscillating local velocity which transports sediment back and forth and may increase the turbidity.
Taking into account the ocean velocity in the wind forcing leads to a decrease of the power lost through friction by the atmosphere, through reducing the relative velocity between the two layers. This result seems to show that the ocean dynamics is important for the energy budget around wind turbines. The results also show that even if the turbulence strongly influences both, ocean and seabed dynamics, its role is negligible in the air-sea energetic balance. Furthermore, as the atmospheric dynamics is not resolved here, the oceanic turbulence has a no retro-action on the atmosphere. Resolving the atmospheric dynamics may further increase the importance of these interactions.

Other processes can be considered with this idealized model by adding tidal currents and time changes in the atmospheric forcing (simulating a storm event) or by including the suspended load sediment transport for example. The parametrization proposed is promising but the determination of the dependence on the confinement deserves further investigation.
To the best of our knowledge, the present work is the first study on the wake interaction with the ocean-sediment dynamics. In contrast, turbine wake models and wind farms interactions with the atmosphere are the subject of a consequent literature. Coupling the present ocean-sediment model with an atmospheric model will increase our understanding of the interaction of a wind turbine with the environment.

Acknowledgements

We thank the Institut Carnot Énergies du Futur and the Observatoire des Sciences de l'Univers de Grenoble (OSUG, LabEx OSUG@2020) for their financial support. All the computations presented in this paper were performed using the Froggy platform of the CIMENT infrastructure (https://ciment.ujf-grenoble.fr), which is supported by the Rhône-Alpes region (GRANT CPER07-13 CIRA) and the Equip@Meso project (reference ANR-10-EQPX-29-01) of the programme Investissements d'Avenir supervised by the Agence Nationale pour la Recherche.

References

[1] EWEA, Deep water, the next step for offshore wind energy, 2013.

[2] K. Dai, A. Bergot, C. Liang, W.-N. Xiang, Z. Huang, Environmental issues associated with wind energy–a review, Renewable Energy 75 (2015) 911–921.

[3] H. Breusers, G. Nicollet, H. Shen, Local scour around cylindrical piers, Journal of Hydraulic Research 15 (3) (1977) 211–252.

[4] H. Breusers, A. Raudkivi, Scouring, Balkema Rotterdam, 1991.

[5] A. Roulund, B. Sumer, J. Fredsøe, J. Michelsen, Numerical and experimental investigation of flow and scour around a circular pile, Journal of Fluid Mechanics 534 (2005) 351–401.

[6] Q. Vanhellemont, K. Ruddick, Turbid wakes associated with offshore wind turbines observed with landsat 8, Remote Sensing of Environment 145 (2014) 105–115.

[7] H. H. Van der Veen, S. Hulscher, B. Perez Lapena, Seabed morphodynamics due to offshore wind farms, in: River, Coastal and Estuarine Morphodynamics: RCEM, 2007.

[8] R. Vautard, F. Thais, I. Tobin, F.-M. Bréon, J.-G. Devezeaux de Lavergne, A. Colette, P. Yiou, P. M. Ruti, Regional climate model simulations indicate limited climatic impacts by operational and planned european wind farms, Nature communications 5.

[9] M. Z. Jacobson, C. L. Archer, W. Kempton, Taming hurricanes with arrays of offshore wind turbines, Nature Climate Change 4 (3) (2014) 195–200.

[10] C. L. Archer, B. A. Colle, L. Monache, M. J. Dvorak, J. Lundquist, B. H. Bailey, P. Beaucage, M. J. Churchfield, A. C. Fitch, B. Kosovic, et al., Meteorology for coastal/offshore wind energy in the united states: recommendations and research needs for the next 10 years, Bulletin of the American Meteorological Society 95 (4) (2014) 515–519.

[11] A. Moulin, A. Wirth, A drag-induced barotropic instability in air–sea interaction, Journal of Physical Oceanography 44 (2) (2014) 733–741.

[12] G. Broström, On the influence of large wind farms on the upper ocean circulation, Journal of Marine Systems 74 (1) (2008) 585591.

[13] Y. Yin, E. Christie, M. Li, C. Moulinec, D. Emerson, 3d morphological impact modelling of offshore wind farms using les and hpc, Coastal Engineering Proceedings 1 (34) (2014) 48.

[14] A. Rivier, A.-C. Bennis, G. Pinon, V. Magar, M. Gross, Parameterization of wind turbine impacts on hydrodynamics and sediment transport, Ocean Dynamics 66 (10) (2016) 1285–1299.

[15] A. B. de Saint-Venant, Théorie du mouvement non permanent des eaux, avec application aux crues des rivieres et a l'introduction des marées dans leurs lits, Comptes Rendus des séances de l'Académie des Sciences 73 (1871) 237–240.

[16] G. K. Vallis, Atmospheric and oceanic fluid dynamics: fundamentals and large-scale circulation, Cambridge University Press, 2006.

[17] H. Schlichting, K. Gersten, E. Krause, H. Oertel, Boundary-layer theory, Springer, 2000.

[18] J. Wu, Wind-stress coefficients over sea surface from breeze to hurricane, Journal of Geophysical Research: Oceans (1978–2012) 87 (C12) (1982) 9704–9706.

[19] S. Smith, Coefficients for sea surface wind stress, heat flux, and wind profiles as a function of wind speed and temperature, Journal of Geophysical Research: Oceans (1978–2012) 93 (C12) (1988) 15467–15472.

[20] R. Deigaard, et al., Mechanics of coastal sediment transport, Vol. 3, World Scientific Publishing Co Inc, 1992.

[21] G. Mellor, P. Durbin, The structure and dynamics of the ocean surface mixed layer, Journal of Physical Oceanography 5 (4) (1975) 718–728.

[22] A. Shields, Anwendung der aehnlichkeitsmechanik und der turbulenzforschung auf die geschiebebewegung, Tech. rep., Preussischen Versuchsanstalt für Wasserbau (1936).

[23] F. M. Exner, Zur physik der dünen, Hölder, 1920.

[24] E. Meyer-Peter, R. Müller, Formulas for bed-load transport, IAHR, 1948.

[25] N. Jensen, A note on wind generator interaction, 1983.

[26] R. G. Ingram, V. H. Chu, Flow around islands in rupert bay: An investigation of the bottom friction effect, Journal of Geophysical Research: Oceans 92 (C13) (1987) 14521–14533.

[27] D. Chen, G. H. Jirka, Experimental study of plane turbulent wakes in a shallow water layer, Fluid dynamics research 16 (1) (1995) 11.

[28] D. Chen, G. H. Jirka, Absolute and convective instabilities of plane turbulent wakes in a shallow water layer, Journal of Fluid Mechanics 338 (1997) 157–172.

[29] A. Moulin, Interaction air-mer à l'échelle synoptique et méso-échelle, Ph.D. thesis, Grenoble Alpes University. HAL Id : tel-01561705 (2015).

[30] G.-S. Jiang, E. Tadmor, Nonoscillatory central schemes for multidimensional hyperbolic conservation laws, SIAM Journal on Scientific Computing 19 (6) (1998) 1892–1917.

[31] G.-S. Jiang, D. Levy, C.-T. Lin, S. Osher, E. Tadmor, High-resolution nonoscillatory central schemes with nonstaggered grids for hyperbolic conservation laws, SIAM Journal on Numerical Analysis 35 (6) (1998) 2147–2168.

[32] V. Marieu, Modélisation de la dynamique des rides sédimentaires générées par les vagues, Ph.D. thesis, Bordeaux 1 (2007).

[33] M. V. Abrahams, M. G. Kattenfeld, The role of turbidity as a constraint on predator-prey interactions in aquatic environments, Behavioral Ecology and Sociobiology 40 (3) (1997) 169–174.

[34] H. Nessyahu, E. Tadmor, Non-oscillatory central differencing for hyperbolic conservation laws, Journal of computational physics 87 (2) (1990) 408–463.

[35] R. J. LeVeque, Finite volume methods for hyperbolic problems, Vol. 31, Cambridge university press, 2002.

Appendix A: Morphodynamic Model description

This section describes the morphodynamic module implemented into the code to solve Exner equation (10). Following [32] work, a conservative shock-capturing schemes has been implemented is the code. But, instead of using, a NOCS (Non-Oscillatory Central Scheme) collocated with the mesh [34] as in [32] work, a NOCS staggered with the mesh has been chosen because it 2D extension was already done by [31]. This type of scheme is able to solve the conservative forms of equations and have a strong stability on shock areas [35]. With the smooth slope shapes finally obtained in 2D simulations it has been decided that local avalanches can not occurs in the present study and therefore no avalanche management module has been added to the morphodynamic model. For notation simplification reason, the seabed elevation denoted previously as h_s is written without it's subscript 's' for the present section.

One Dimensional NOCS Staggered Scheme

The NOCS scheme solves the Exner equation in two steps: a predictor-step, that gives a temporary bedform from which fluxes are recalculated and the corrector-step in which the definitive bedform is obtained.
The predictor step gives the bed elevation at grid point i after one half time-step calculation (n+1/2):

$$ {h_i}^{n+\frac{1}{2}} = {h_i}^{n} - \frac{1}{2}\frac{\delta t}{\delta x}\, {q_i}' \ , \tag{A.1} $$

where ${q_i}'$ is the sediment flux derivative approximation at grid point i. The temporary flux depends only on the bed elevation ${h_i}^{n+\frac{1}{2}}$:

$$ {q_i}^{n+\frac{1}{2}} = q\left({h_i}^{n+\frac{1}{2}}\right) \ , \tag{A.2} $$

The calculation of ${q_i}'$ and ${h_i}'$ involves a slope limiter, in order to ensure TVD (Total Variation Diminishing) properties of the solution. In the present work,

$\beta-$limiter has been used. In order to compute the derivative approximation of a function ϕ, the $\beta-$limiters are define as follow:

$$\phi_i{}' = \text{MinMod}\left[\beta(\phi_\text{i} - \phi_\text{i-1}),\ \frac{1}{2}(\phi_\text{i+1} - \phi_\text{i-1}),\ \beta(\phi_\text{i+1} - \phi_\text{i})\right]\ , \tag{A.3}$$

where β is the limiter parameter and $MinMod$ the function such as:

$$\text{MinMod}\{\text{x}_1, \text{x}_2, \text{x}_3\} = \begin{cases} min\{x_1, x_2, x_3\} & if\ x_k > 0;\ \forall k = 1, 2, 3, \\ max\{x_1, x_2, x_3\} & if\ x_k < 0;\ \forall k = 1, 2, 3, \\ 0 & \text{else} \end{cases} \tag{A.4}$$

when $\beta = 1$, the limiter is the so-called $MinMod$ and when $\beta = 2$ it is the *Superbee* limiter, the latter is less diffusive.

The corrector is on a staggered grid and it is based on the reconstruction of a piecewise-linear interpolant from the known staggered cell-averages at time t^n:

$$\bar{h}(x, t^n) = \sum_i \left[{h_i}^n - {h_i}'\left(\frac{x - x_i}{\Delta x}\right)\right]\chi_i(x), \tag{A.5}$$

where ${h_i}'$ is the discrete slope involving the slope limiter described in equations A.3 and A.4, and where $\chi_i(x)$ is the characteristic function of the cell $I_i := \mid x - x_i \mid \leq \Delta x/2$.
This interpolant is then projected on the staggered cell-averages on the next time step, t^{n+1}:

$${h_{i+\frac{1}{2}}}^{n+1} = \frac{1}{2}\left({h_i}^n + {h_{i+1}}^n\right) + \frac{1}{8}\left({h_i}' - {h_{i+1}}'\right) - \frac{\delta t}{\delta x}\left({q_{i+1}}^{n+\frac{1}{2}} - {q_i}^{n+\frac{1}{2}}\right), \tag{A.6}$$

The staggered corrector has to be reprojected on the non-staggered grid by using a piecewise-linear interpolant through the calculated staggered cell-averages at time t^{n+1}:

$$\bar{h}_{i+\frac{1}{2}}{}^{n+1} = {h_{i+\frac{1}{2}}}^{n+1} - {h_{i+\frac{1}{2}}}'\left(\frac{x - x_{i+\frac{1}{2}}}{\Delta x}\right), \tag{A.7}$$

where ${h_{i+\frac{1}{2}}}'$ is the staggered discrete derivative of the staggered corrector term. Finally, the cell-averages at time t^{n+1} are obtained by averaging this interpolant,resulting in the non-staggered corrector scheme:

$$\begin{aligned} {h_i}^{n+1} = & \frac{1}{\Delta x}\left[\int_{x_{i-\frac{1}{2}}}^{x_i} \bar{h}_{i-\frac{1}{2}}{}^{n+1} + \int_{x_i}^{x_{i+\frac{1}{2}}} \bar{h}_{i+\frac{1}{2}}{}^{n+1}\right] \\ {h_i}^{n+1} = & \frac{1}{4}\left({h_{i-1}}^n - 2{h_i}^n + {h_{i+1}}^n\right) - \frac{1}{16}\left({h_{i+1}}' - {h_{i-1}}'\right) - \frac{1}{8}\left({h_{i+\frac{1}{2}}}' - {h_{i-\frac{1}{2}}}'\right) \\ & - \frac{\delta t}{2\delta x}\left({q_{i+1}}^{n+\frac{1}{2}} - {q_i}^{n+\frac{1}{2}}\right) \end{aligned} \tag{A.8}$$

Figure 3.1 from [31] shows the second order construction process leading to the non-staggered corrector scheme and may be useful to the reader.
For staggered variables, boundary conditions slightly differ from the ones described in section 3.2. Indeed, as the grid is staggered extreme points are out of the domain. In 1D, the non staggered grid has the size n, while the staggered one has the size $n+1$, starting from 0 to n. For a given f function, periodic boundary conditions are given by:

$$\begin{gathered} f(0) = f(n-2) \\ f(n) = f(2) \\ f(n-1) = f(1) \end{gathered}$$

Two Dimensional Extension

The arguments applied in the one-dimensional case can be easily extended to higher dimensions. This extension is straightforward and is based on exactly the same procedure described in the previous section. A non-staggered scheme is created from a staggered scheme by averaging the interpolants constructed from the given staggered values. In two dimensions, predictor and staggered corrector become respectively:

$$h_{i,j}{}^{n+\frac{1}{2}} = h_{i,j}{}^{n} - \frac{1}{2}\frac{\delta t}{\delta x}\, qx_{i,j}{}' - \frac{1}{2}\frac{\delta t}{\delta y}\, qy_{i,j}{}' \,, \tag{A.9}$$

where $qx_{i,j}{}'$ and $qy_{i,j}{}'$ are the flux derivative approximation in the x and y directions respectively.

$$\begin{aligned} h_{i+\frac{1}{2},j+\frac{1}{2}}{}^{n+1} = \; & \frac{1}{4}\left(h_{i,j}{}^{n} + h_{i+1,j}{}^{n} + h_{i,j+1}{}^{n} + h_{i+1,j+1}{}^{n}\right) \\ & + \frac{1}{16}\left(h'_{i,j} + h'_{i+1,j} + h'_{i,j+1} + h'_{i+1,j+1}\right) \\ & + \frac{1}{16}\left(h`_{i,j} + h`_{i+1,j} + h`_{i,j+1} + h`_{i+1,j+1}\right) \\ & - \frac{\delta t}{2\delta x}\left(qx_{i+1,j}{}^{n+\frac{1}{2}} - qx_{i,j}{}^{n+\frac{1}{2}} + qx_{i+1,j+1}{}^{n+\frac{1}{2}} - qx_{i,j+1}{}^{n+\frac{1}{2}}\right) \\ & - \frac{\delta t}{2\delta y}\left(qy_{i,j+1}{}^{n+\frac{1}{2}} - qy_{i,j}{}^{n+\frac{1}{2}} + qy_{i+1,j+1}{}^{n+\frac{1}{2}} - qy_{i+1,j}{}^{n+\frac{1}{2}}\right) \end{aligned} \tag{A.10}$$

The prime and back-prime notation denote the discrete derivatives in the x and y directions, respectively. The piecewise-linear interpolant reconstruction is then averaged, resulting in the non-staggered corrector at time step t^{n+1} and

in cell $I_{i,j}$:

$$
\begin{aligned}
{h_{i,j}}^{n+1} = \quad & \frac{1}{4\Delta x \Delta y}\left[\int\int_{I_{i+\frac{1}{2},j+\frac{1}{2}}} {\bar{h}_{i+\frac{1}{2},j+\frac{1}{2}}}^{n+1} + \int\int_{I_{i-\frac{1}{2},j+\frac{1}{2}}} {\bar{h}_{i-\frac{1}{2},j+\frac{1}{2}}}^{n+1}\right] + \\
& \frac{1}{4\Delta x \Delta y}\left[\int\int_{I_{i-\frac{1}{2},j-\frac{1}{2}}} {\bar{h}_{i-\frac{1}{2},j-\frac{1}{2}}}^{n+1} + \int\int_{I_{i+\frac{1}{2},j-\frac{1}{2}}} {\bar{h}_{i+\frac{1}{2},j-\frac{1}{2}}}^{n+1}\right] \\
{h_{i,j}}^{n+1} = \quad & \frac{1}{4}\left({h_{i+\frac{1}{2},j+\frac{1}{2}}}^{n+1} + {h_{i-\frac{1}{2},j+\frac{1}{2}}}^{n+1} + {h_{i-\frac{1}{2},j-\frac{1}{2}}}^{n+1} + {h_{i+\frac{1}{2},j-\frac{1}{2}}}^{n+1}\right) \\
& + \frac{1}{16}\left[\left(h'_{i-\frac{1}{2},j-\frac{1}{2}} - h'_{i+\frac{1}{2},j-\frac{1}{2}}\right) + \left(h'_{i-\frac{1}{2},j+\frac{1}{2}} - h'_{i+\frac{1}{2},j+\frac{1}{2}}\right)\right] \\
& + \frac{1}{16}\left[\left(h`_{i-\frac{1}{2},j-\frac{1}{2}} - h`_{i-\frac{1}{2},j+\frac{1}{2}}\right) + \left(h`_{i+\frac{1}{2},j-\frac{1}{2}} - h`_{i+\frac{1}{2},j+\frac{1}{2}}\right)\right]
\end{aligned}
\tag{A.11}
$$

The two-dimensional staggered (red) and non staggerred (black) grids are sketched on figure A.1, adapted from [31].

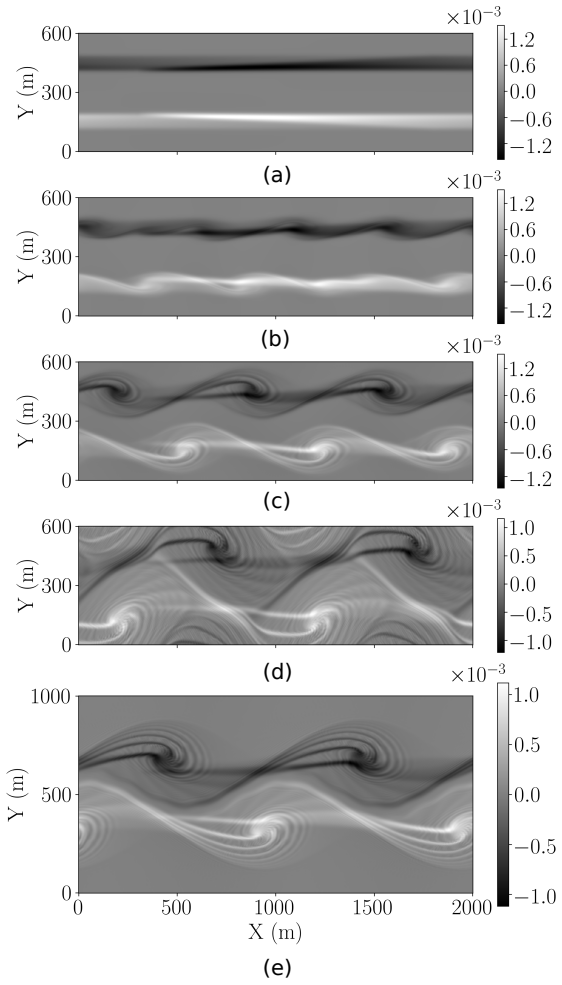

Figure 3: 2D vorticity fields after 14 days of dynamics for H15, (a) H20 (b), H30 (c), H50 (d) and H50w (e). Increasing the water layer thickness leads to a generation of two types of oceanic instabilities, distincts and interacting ones. This instabilities generation is controled by the wake stability parameter S.

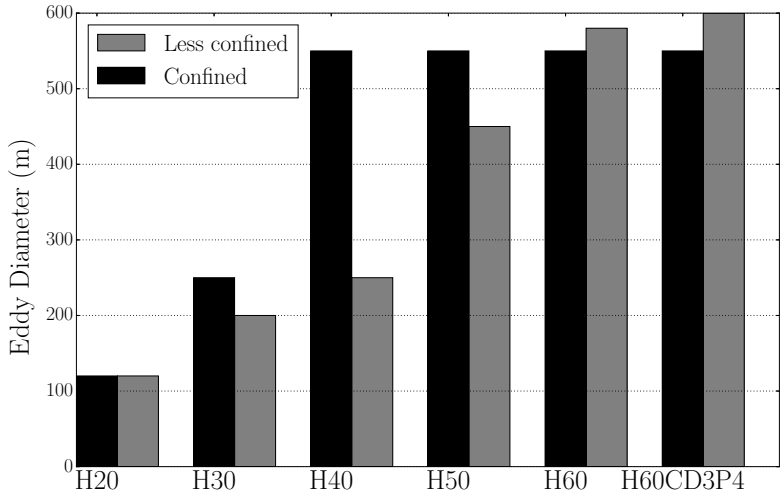

Figure 4: Comparison between the eddies diameter for the different numerical simulations undertaken.

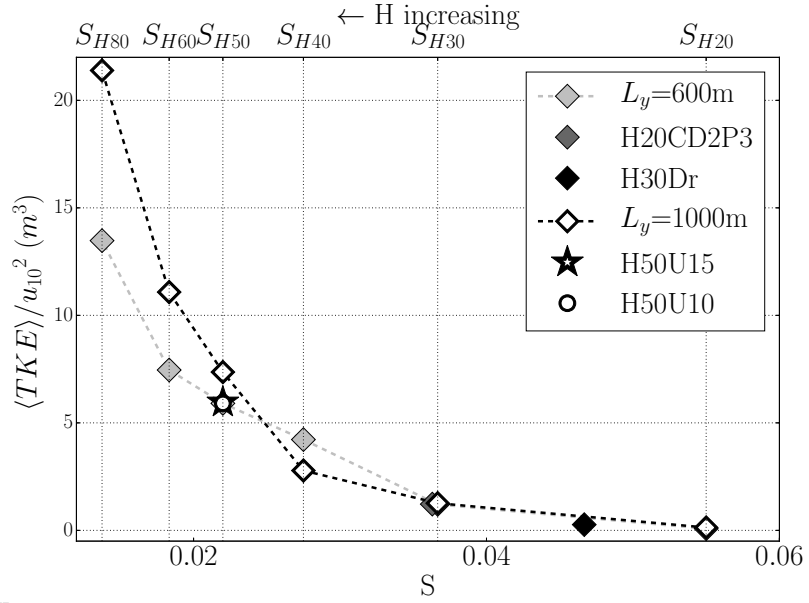

Figure 5: Plot of the normalized TKE as a function of the S parameter. Full and empty diamonds symbols correspond to confined (H15, H20, H30, H40, H50, H60, H60CD2P3) and less-confined (H20w, H30w, H40w, H50w, H60w, H60wCD2P3) cases, respectively. The wake stability parameter is a control parameter of the oceanic turbulent dynamic, even if a dependency on the domain width remains.

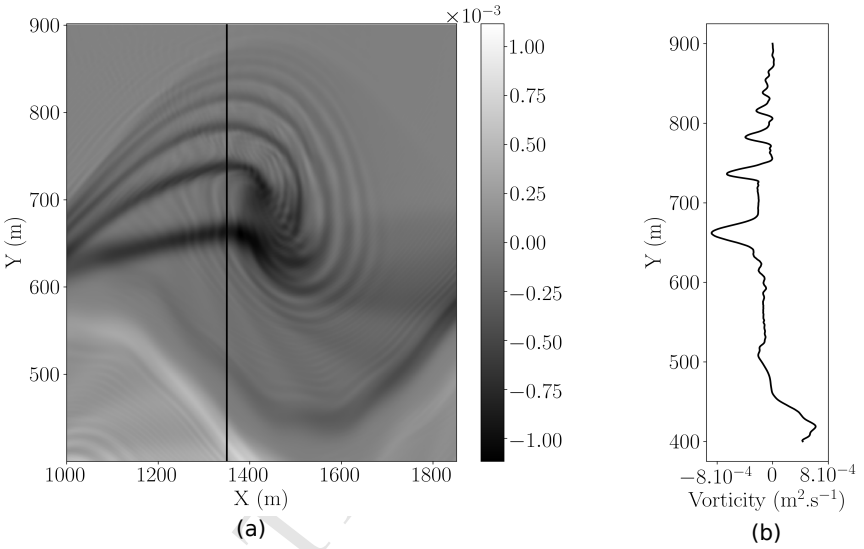

Figure 6: Zoom (a) and transect along the y-direction (b) of an eddy presented in figure 3, for the H50w case. The spaghetti-type structure of the vorticity field induced by atmospheric wake forcing and periodic boundary conditions but also the decaying vorticity intensity of the rotated filaments are clearly identifiable in the transect plot.

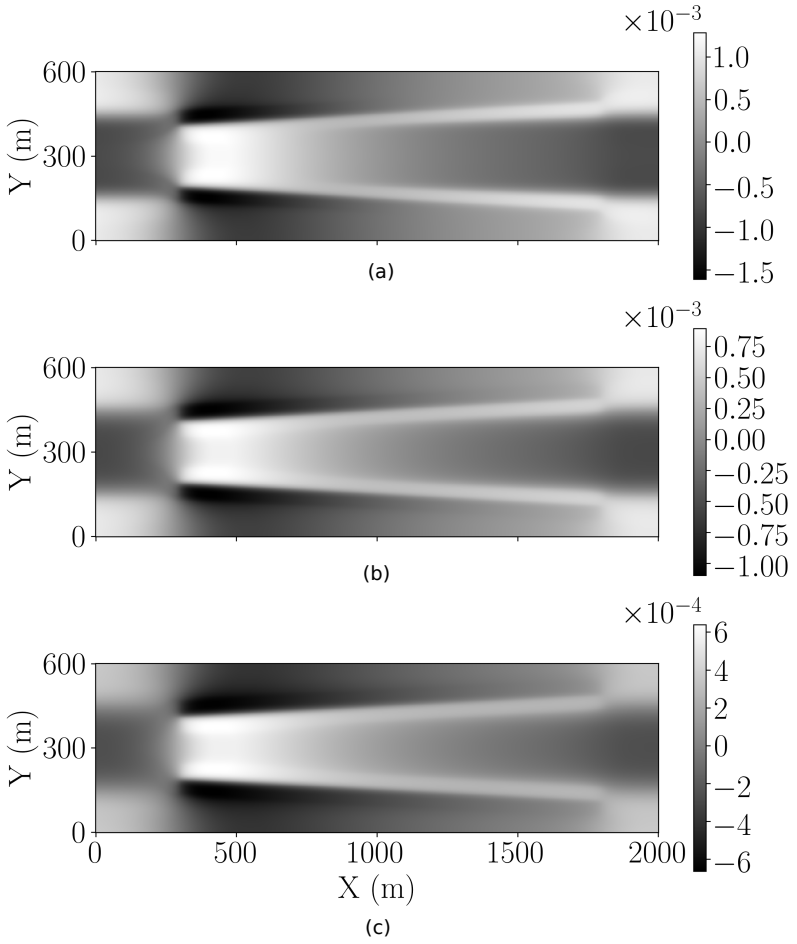

Figure 7: Seabed elevation after 14 days of dynamics for H20 (a), H30 (b) and H50 (c). The non-uniformity of the oceanic velocity field induced by the wake presence is recovered in the local bottom shear stress responsible for sand erosion and deposition.

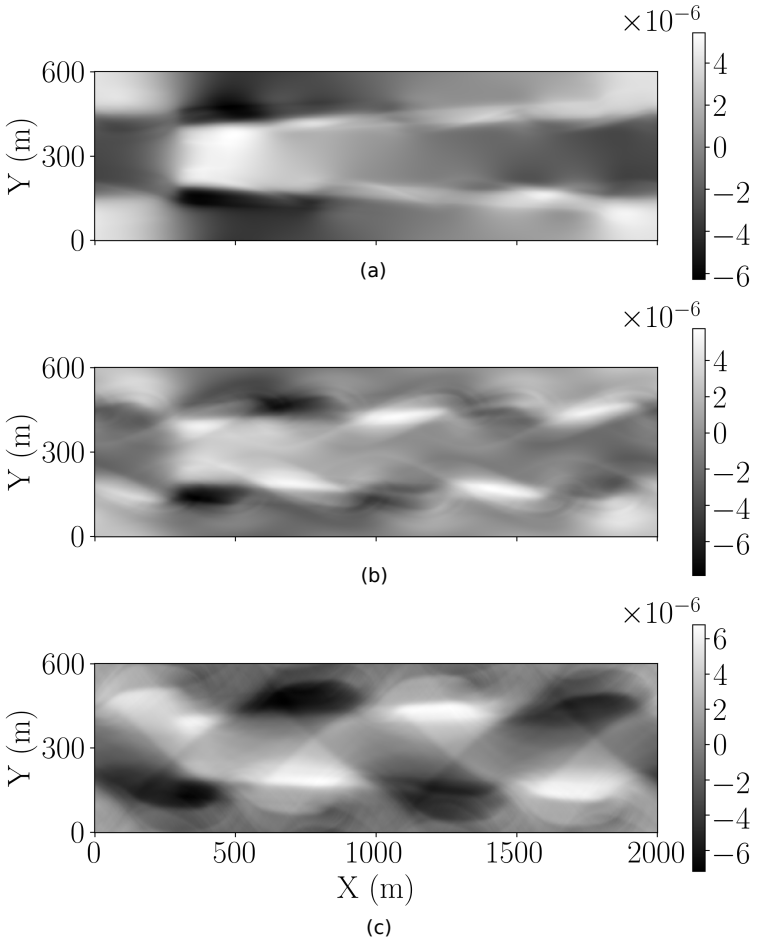

Figure 8: Short term seabed elevation changes, Δt =4000 s, for H20 (a), H30 (b) and H50 (c). As the vortices strongly affect the seabed morphodynamics, for localized (b) and domain wide turbulence (c), the wakes imprint tends to be reduced by large scale vortices and the oscillating local velocity which transports sediments back and forth.

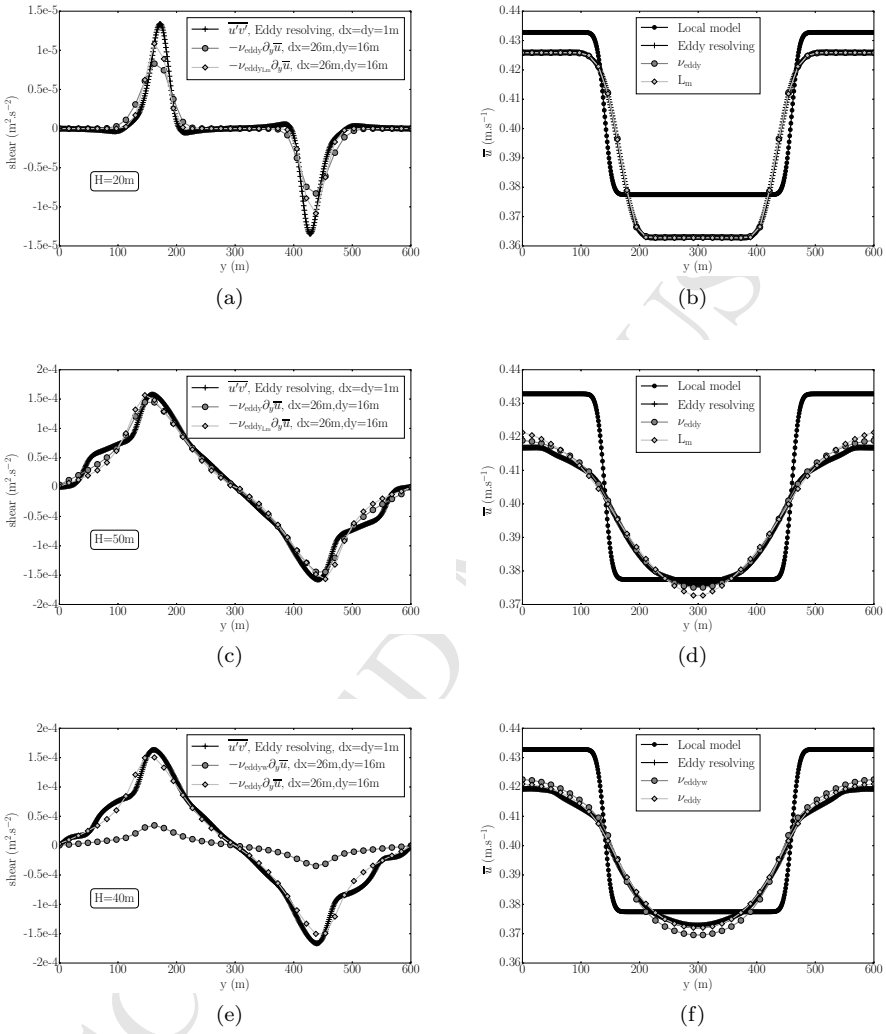

Figure 9: Confined runs y− direction transect at x=1300m of the shear (a,c,e) and mean velocity field $\overline{u}$ (b,d,f) for different water layer thicknesses. Eddy resolving computations (cross) and the three parametrizations are represented. For the 40m water layer thickness case (e,f), the circles symbols show the results obtained with an eddy viscosity computed from the non-confined configuration, when the diamonds curve is obtained with a eddy viscosity computed from the confined configuration. The results are satisfactory on the mean velocity field $\overline{u}$, but they are incorrects on the shear.

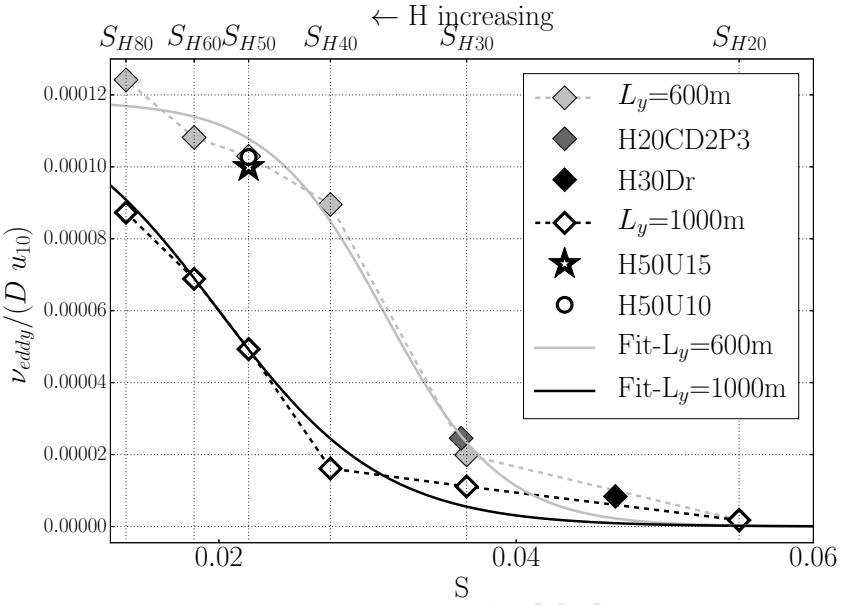

Figure 10: Plot of the non-dimensionalized ν_{eddy} as a function of the S parameter. For a given domain width, ν^*_{eddy} collapses on a curve as a function of the S parameter and can be fitted by a hyperbolic tangent function of S. Full and empty diamonds symbols correspond to confined (H15, H20, H30, H40, H50, H60, H60CD2P3) and less-confined (H20w, H30w, H40w, H50w, H60w, H60wCD2P3) cases, respectively.

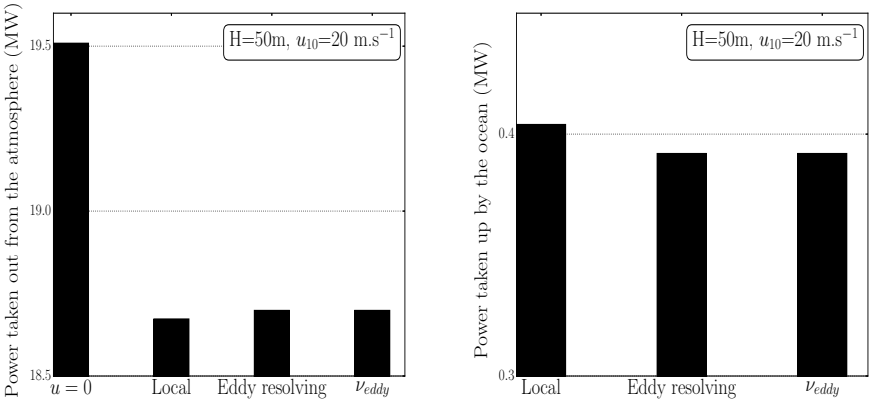

Figure 11: Comparison of the power taken out from the atmosphere (a) and the one taken up by the ocean (b) for the different models. Case presented here is H50.

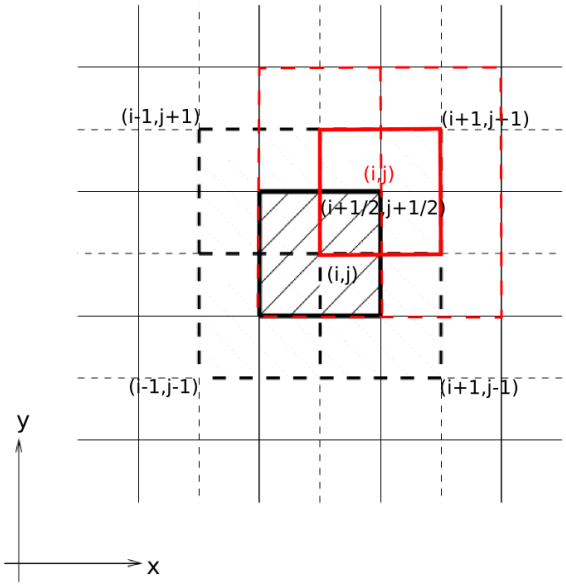

Figure A.1: Two-dimensional staggered (red) and non staggerred (black) grids. Adapted from [31].

- The turbine wake has an impact on both the ocean and the seabed dynamics.
- The turbine wake impact on the ocean surface generate instabilities and vortex streets.
- A phenomenological law for the non−dimensional eddy viscosity has been proposed.
- The wake presence is responsible for seabed sand erosion and deposition.
- The ocean dynamics is important for the energy budget around wind turbines.